Published in final edited form as:
Sci Signal. ; 6(283): ra56. doi:10.1126/scisignal.2003649.

Regulators of Calcium Homeostasis Identified by Inference of Kinetic Model Parameters from Live Single Cells Perturbed by siRNA

Samuel Bandara[*,†], **Seth Malmersjö**, and **Tobias Meyer**[*]
Department of Chemical and Systems Biology, Stanford University, Stanford, CA 94305, USA

Abstract

Assigning molecular functions and revealing dynamic connections between large numbers of partially characterized proteins in regulatory networks are challenges in systems biology. We showed that functions of signaling proteins can be discovered with a differential equations model of the underlying signaling process to extract specific molecular parameter values from single-cell, time-course measurements. By analyzing the effects of 250 small interfering RNAs on Ca^{2+} signals in single cells over time, we identified parameters that were specifically altered in the Ca^{2+} regulatory system. Analysis of the screen confirmed known functions of the Ca^{2+} sensors STIM1 (stromal interaction molecule 1) and calmodulin and of Ca^{2+} channels and pumps localized in the endoplasmic reticulum (ER) or plasma membrane. Furthermore, we showed that the Alzheimer's disease–linked protein presenilin-2 and the channel protein ORAI2 prevented overload of ER Ca^{2+} and that feedback from Ca^{2+} to phosphatidylinositol 4-kinase and PLCδ (phospholipase Cδ) may regulate the abundance of the plasma membrane lipid $PI(4,5)P_2$ (phosphatidylinositol 4,5-bisphosphate) to control Ca^{2+} extrusion. Thus, functions of signaling proteins and dynamic regulatory connections can be identified by extracting molecular parameter values from single-cell, time-course data.

INTRODUCTION

Mammalian signal transduction relies on feedback-connected regulatory networks that integrate cues from both the inside and outside of cells to control specific cell functions. The quest to assign molecular functions and to reveal dynamic connections between large numbers of putative or partially characterized proteins in such a network is formidable because only a limited number of molecular parameters can be monitored in live cells. Here, we exploited the fact that a measured time course of a cell's response is differentially shaped by multiple underlying molecular parameters, such that the response trajectory reflects changes in internal states and activities that are otherwise difficult to measure. Extraction of hidden parameters from time-resolved measurements using ordinary differential equations has been applied in engineering. In biology, this parameter extraction approach has been used to interpret population dynamics, such as the kinetics of viral load (1) or bacterial growth (2), and to analyze phosphorylation kinetics from bulk cell measurements (3).

[*]Corresponding author. sbandara@alumni.stanford.edu (S.B.); tobias1@stanford.edu (T.M.).
[†]Present address: Department of Systems Biology, Harvard Medical School, Boston, MA 02115, USA.

Author contributions: S.B. and T.M. conceived the study; S.B. and S.M. performed the experiments and analyzed the data; and S.B., S.M., and T.M. wrote the manuscript.

Competing interests: T.M. is a member of the scientific advisory board of Molecular Devices, Sunnyvale, CA. All other authors declare that they have no competing interests.

However, the comprehensive use of parameter estimation in an entire signaling system is challenged by potentially incomplete model structures and the need to identify experimental protocols that sufficiently constrain model parameters (4). Moreover, the reaction rates of a signaling system often depend nonlinearly on the concentrations of signaling molecules that vary considerably from cell to cell. Therefore, population-averaged time courses not only blunt characteristic features of single-cell responses, such as the steepness, curvature, or peak time of a signaling trajectory, but the combination of nonlinearity with in-herent variability also precludes the accurate representation of a population-averaged signal trajectory by a molecular kinetic model. Therefore, we asked whether a kinetic model can instead be constrained by analyzing large numbers of variable single-cell trajectories. Such a strategy is becoming broadly applicable with the increased availability of automated live-cell imaging and with the availability of massively parallel computing of numerically stable algorithms for parameter estimation, such as the multiple-shooting method (5), which we used here. Combined with systematic small interfering RNA (siRNA) perturbations, this model-based analysis of single-cell dynamics allowed us to identify molecular roles of putative regulatory proteins and to reconstruct control principles of a complex signaling system using a single scalable assay.

We applied this approach to mammalian Ca^{2+} signaling because of the documented complexity of regulation that governs a core system of pumps and channels (Fig. 1). This core part of the cellular Ca^{2+} system can be engaged by numerous types of receptors that open Ca^{2+} channels in the plasma membrane (PM) or endoplasmic reticulum (ER) (6). PM Ca^{2+} pumps (PMCA1, PMCA2, PMCA3, PMCA4) extrude Ca^{2+} to the outside, maintaining a basal cytosolic concentration of ~70 nM against an extracellular concentration of 1.5mM, and ER Ca^{2+} pumps (SERCA1, SERCA3,SERCA3) load Ca^{2+} into the ER to ~400 μM, which is available for receptor-triggered release through inositol trisphosphate–sensitive Ca^{2+} channels [IP_3Rs (inositol 1,4,5-trisphosphate receptors)]. Both types of pumps counter the effect of leak through constitutively active Ca^{2+} leak channels, as well as Ca^{2+} signals arising from activation of channels in the ER and the PM. The ER and PM are connected by feedback through a family of Ca^{2+}-binding STIM (stromal interaction molecule) proteins that sense decreased ER Ca^{2+} concentrations to induce PM Ca^{2+} influx through activation of ORAI Ca^{2+} channels [store-operated Ca^{2+} influx (SOC)] (7).

RESULTS

Quantitative model to probe the Ca^{2+} regulatory system

We rapidly chelated extracellular Ca^{2+} with EGTA to prevent Ca^{2+} influx and added thapsigargin to inhibit ER SERCA pumps (8), and then using the cytosolic Ca^{2+} indicator Fluo-4, we monitored the resulting release of Ca^{2+} from ER Ca^{2+} stores into the cytoplasm and its clearance out of the cell (Fig. 2A). For each cell, we also measured SOC (k_{SOC}) by addition of external Ca^{2+} (7) at the end of the experiment. The response of individual cells after EGTA and thapsigargin treatment was highly variable, as shown by substantial coefficients of variation for amplitudes and peak times (Fig. 2, B and C).

We developed a quantitative model that describes the resulting single-cell responses (change in the concentration of cytosolic Ca^{2+} $[Ca^{2+}]_{cyt}$) as the result of a leak of Ca^{2+} out of the ER into the cytosol at a rate $k_{ER,leak}$ and the pumping of Ca^{2+} from the cytoplasm to the outside with a capacity J_{max}, an affinity K_M, and cooperativity n (9). We used the measured Fluo-4 intensity to derive $[Ca^{2+}]_{cyt}$, assuming saturable Ca^{2+} binding and a residual fluorescence F_{min} in the absence of Ca^{2+} (Fig. 2D).

Model calibration using a multiple-shooting Gauss-Newton–type algorithm (5)with all seven parameters left open resulted in close agreement between model output and individual

single-cell trajectories (Fig. 2A). Moreover, the average parameter estimates obtained from large numbers of individual single-cell traces agreed well with previously reported values (Fig. 2E; see Materials and Methods). However, the parameters of individual cells were poorly defined and co-dependent (Fig. 2F and fig. S1, A and B). For example, two of the insets in Fig. 2F (upper right and lower left) show examples in which parameter combinations within the blue-shaded region correspond to virtually identical fits despite more than 10-fold differences in parameter values. Additionally, even small deviations from this region generated highly discrepant predictions (Fig. 2F, upper left insert). We considered that the regulated parameters would be better constrained (that is, the region in parameter space that matched the response trajectory would be more limited) if the invariant parameters n, K_M, and F_{min} were constrained independently on the basis of previous knowledge (Fig. 2F, red-shaded region). However, the challenge of such an approach is that even small errors in fixing the invariant parameters would preclude any possible fit, rendering all other parameters inaccessible for analysis [fig. S1B; see also (4)].

The uncertainty of parameter estimates can also be described by a local approximation of the covariance matrix based on the sensitivity of measurement predictions to parameter values (10). Such calculations showed that a predominant direction, or eigenvector, in parameter space exists, along which parameter values are uncertain (fig. S1C). This direction spans several of the parameter axes and constitutes, for example, the negative correlation of $k_{ER,leak}$ and $[Ca^{2+}]_{ER}(0)$ seen in Fig. 2F (indicated in fig. S1C by a difference in sign of the corresponding components) and correlations of these parameters with invariant parameters, such as F_{min}. This interdependence explains why previous knowledge of one invariant parameter can constrain estimates of other parameters. In particular, such calculations predicted that if n, K_M, and F_{min} were known, then the regulated parameters J_{max}, $Ca^{2+}{}_{ER}(0)$, and $k_{ER,leak}$ would be well determined even if PMCA or, to a lesser degree, SERCA was knocked down (fig. S1, D and E).

Predicting protein function from single-cell, time-resolved siRNA data using a kinetic model

We established cocultures of human embryonic kidney (HEK) 293T cells transfected with siRNAs to knock down proteins of interest and fluorescently marked control cells and used these cocultured cells to obtain model-derived estimates for n, K_M, and F_{min}. We analyzed large numbers of single-cell responses of control cells cultured in conditions identical to those of the siRNA-targeted cells. Although poorly defined when estimated from individual cells, we used the average estimates of these invariant parameters obtained from hundreds of individual control cells per well to constrain a second round of single-cell parameter estimation in both the control and the siRNA-targeted cells (Fig. 3A, see Materials and Methods). Overlaying the model trajectories on the experimental single-cell responses after PMCA1 or SERCA2 knockdown (Fig. 3, B and C) showed that the constrained model retained its ability to recapitulate variable single-cell responses and that it could do so in different siRNA perturbation backgrounds.

Moreover, decomposing the single-cell time courses into distinct molecular parameters correctly assigned the known cellular roles to the PMCA and SERCA Ca^{2+} pumps. Only J_{max} was reduced in cells in which PMCA1 was knocked down (Fig. 3D). The PMCA1 knockdown cells also had increased basal $[Ca^{2+}]_{cyt}$ (Fig. 3D, third graph) and showed adaptive down-regulation of SOC (Fig. 3D, fourth graph) as previously observed in insect cells (11). Likewise, knockdown of SERCA2 predominantly reduced the ER load $[Ca^{2+}]_{ER}(0)$, but not J_{max}, and also resulted in increased basal $[Ca^{2+}]_{cyt}$ due to the feedback activation of SOC (Fig. 3E). Together, this showed that parameter shifts induced by siRNAs

targeting proteins that function in the regulatory network can directly predict protein function and provide insight into mechanisms of adaptation.

Identifying function from dynamic siRNA perturbation data

We extended this analysis to an siRNA set targeting 250 known or putative regulators of Ca^{2+} (table S1).We plotted the effects of the siRNAs on k_{SOC} (Fig. 4A), $[Ca^{2+}]_{ER}(0)$ (Fig. 4B), $k_{ER,leak}$ (Fig. 4C), or J_{max} (Fig. 4D) against the siRNA-evoked changes of basal $[Ca^{2+}]_{cyt}$ that we measured before adding thapsigargin and EGTA. We calculated all changes as log-fold changes relative to the control cells that we cultured in each well (table S2), median-centered and normalized by the SD along each dimension per independent replicate screen. When analyzing the effect of the perturbation set on k_{SOC}, we observed a significant correlation with basal $[Ca^{2+}]_{cyt}$ (Fig. 4A). The two canonical SOC molecules STIM1 and ORAI1 were at the lower left of the distribution, indicating that knockdown of either of these proteins reduced basal $[Ca^{2+}]_{cyt}$ and reduced SOC compared to control cells. In contrast, we observed an anticorrelation between the ER Ca^{2+} load and $[Ca^{2+}]_{cyt}$ (Fig. 4B). Our finding that not only reductions in $[Ca^{2+}]_{ER}$ but also increases led to opposing changes in $[Ca^{2+}]_{cyt}$ indicated that SOC also operates in cells at rest (12).

Although knockdown of the ER Ca^{2+} pump SERCA2 produced the largest decrease in ER Ca^{2+}, one of the presenilin-2 (encoded by *PSEN2*) knockdowns produced a large increase in ER Ca^{2+} load. Presenilins are the catalytically active constituent of the γ-secretase complex (13), and mutations in *PSEN2* are associated with familial cases of Alzheimer's disease (14). Loss of presenilin function has been proposed to either increase or decrease $[Ca^{2+}]_{ER}$ (15–17), or not to change $[Ca^{2+}]_{ER}$ (18). Given the current controversy, we tested the predicted physiological role of PSEN2 in regulating ER Ca^{2+} load using a fluorescence resonance energy transfer (FRET) probe based on the design of D1ER to measure changes in ER Ca^{2+} directly (11). Knockdown of PSEN2 significantly increased ER Ca^{2+} load when compared to control cells (Fig. 4E and fig. S2), and overexpression of PSEN2 resulted in the opposite effect (Fig. 4F).

Knockdown of presenilin enhancer 2 homolog (encoded by *PSENEN*), which is required for the proteolytic processing of presenilins (19), yielded a large increase in $k_{ER,leak}$, whereas knockdown of PSEN2 decreased $k_{ER,leak}$ (Fig. 4C). Such a role of PSENEN in reducing $k_{ER,leak}$ may be due to its function in reducing the amount of unprocessed PSEN2 (19), because the unprocessed form of presenilins contributes to ER Ca^{2+} leak (15, 17). However, knock-down of the ER Ca^{2+} release channel IP_3R1 (encoded by *ITPR1*) or ORAI2 also had strong effects on $k_{ER,leak}$ (Fig. 4C). Although the identification of IP_3R1 is consistent with previous observations of a basal activity of IP_3Rs (16), a function for ORAI2 in ER Ca^{2+} leak has previously not been described. We used the ER Ca^{2+} FRET probe to measure changes of ER Ca^{2+} in cells in which ORAI2 was knocked down or overexpressed. Knockdown of ORAI2 significantly increased $[Ca^{2+}]_{ER}$ (Fig. 4E), whereas overexpression had the opposite effect (Fig. 4F). Because ORAI2 fails to rescue SOC in ORAI1 knockout cells (20),we confirmed further that the observed decrease in $[Ca^{2+}]_{ER}$ was not due to a dominant-negative effect of the overexpressed ORAI2 on SOC entry by measuring basal $[Ca^{2+}]_{cyt}$. In cells overexpressing ORAI2, basal $[Ca^{2+}]_{cyt}$ was increased as expected for an ER Ca^{2+} leak channel that triggers SOC as a result of lowering of $[Ca^{2+}]_{ER}$ under basal conditions (fig. S3). Thus, our findings suggested that the ER Ca^{2+} leak may result from the cumulative conductance of many proteins, including unprocessed presenilins, basally active IP_3Rs, and Ca^{2+} channels, such as ORAI2, that conduct Ca^{2+} as they progress through the ER en route to the PM.

The effect of the perturbation set on the inferred extrusion capacity J_{max} was anti-correlated with basal $[Ca^{2+}]_{cyt}$ (Fig. 4D), with multiple targeted proteins affecting Ca^{2+} extrusion.

Large parameter shifts were caused by knockdown of the PMCA isoform encoded by *PMCA1* or knockdown of calmodulin isoforms encoded by *CALM1* or *CALM2*, consistent with a critical role of calmodulin in PMCA activation (6). We identified two additional Ca^{2+}-binding proteins, hippocalcin (encoded by *HPCA*) and neuronal calcium sensor-1 (NCS1; a homolog of the fly and yeast Ca^{2+}-binding protein frequenin), as putative regulators of Ca^{2+} extrusion. Although a role for hippocalcin in Ca^{2+} extrusion from hippocampal neurons has been suggested previously (21), *Saccharomyces cerevisiae* frequenin and NCS1 have been shown to function as Ca^{2+}-activated positive regulators of phosphatidylinositol (PI) 4-kinase, which converts PI to PI(4)P (phosphatidylinositol 4-phosphate) (22, 23).

Identifying a role for $PI(4,5)P_2$ in regulation of Ca^{2+} extrusion

Consistent with a regulatory role for NCS1 at the PM, we observed a small but significant increase in the PM localization of an NCS1-mCherry fusion protein after cytosolic Ca^{2+} was increased by addition of ionomycin and extracellular Ca^{2+} (Fig. 5, A and B, and movie S1). Because PI(4)P is the main precursor of $PI(4,5)P_2$ (phosphatidylinositol 4,5-bisphosphate), it was intriguing to also identify phospholipase Cδ3 (PLCδ3; encoded by *PLCD3*), which hydrolyzes PI(4,5) lipids, as a strong regulator opposing Ca^{2+} extrusion (Fig. 4D). $PI(4,5)P_2$ is required in reconstituted membranes for purified PMCA to be active (24); thus, the effects of knocking down NCS1 or PLCδ3 may result from altering $PMPI(4,5)P_2$ and thereby affecting PMCA activity.

To test whether $PI(4,5)P_2$ enhanced PMCA activity in a cellular context, we lowered the concentration of $PI(4,5)P_2$ by expressing a fusion protein containing the catalytic domain of the $PI(4,5)P_2$ 5-phosphatase (INP54P) from *S. cerevisiae* in HeLa cells. Indeed, Ca^{2+} that was rapidly released from the ER by addition of ionomycin and thapsigargin in the presence of extracellular EGTA was eliminated at a twofold slower rate from cells expressing INP54P than from control cells (Fig. 5C). Thus, the regulation of PMCA activity by $PI(4,5)P_2$ revealed a network with two feedbacks by which Ca^{2+}-mediated activation of NCS1 increases and activation of PLCδ3 reduces the concentration of $PI(4,5)P_2$.

DISCUSSION

Our understanding of signal transduction systems is challenged by a high degree of variation of signaling responses within a cell population and by the limited number of reporters available to track specific signaling events over time. Our study showed that a single signaling reporter, combined with rapid perturbation and a mechanistically explicit differential equations model, can be used to determine multiple molecular parameters from single-cell data even for a complex signaling system.

The value of single-cell traces over population-averaged traces for our analysis method is exemplified by considering the extrusion term in our model. We found in our analysis of variability (Fig. 2, A to C) that cells have peak cytosolic Ca^{2+} concentrations as different as ~600 and ~200 nM shortly after addition of thapsigargin and EGTA. The instantaneous flux rate of extrusion for these cells calculates to 7.73 and 4.25 nM/s, respectively. On average, cytosolic Ca^{2+} will be extruded out of these cells at a rate of 5.99 nM/s. However, extrusion calculated on the basis of the average concentration of cytosolic Ca^{2+} at 400 nM calculates to 6.89 nM/s. This discrepancy is due to cooperativity and saturation (Fig. 2D, term labeled “2”) and would result in a substantial error in inferring other values in the same equation, such as the cooperativity of the PM Ca^{2+} pump or the ER leak rate. Thus, for a nonlinear process with high cell-to-cell variability, only single-cell data can accurately constrain the parameters of a kinetic model.

We combined this approach with systematic siRNA perturbations to reconstruct the regulatory control principles of the Ca^{2+} homeostatic system and assign molecular roles to putative regulatory proteins. Most notably, our analysis revealed a role of $PI(4,5)P_2$ in controlling the rate of Ca^{2+} extrusion, confirmed a controversial hypothesis that PSEN2 has a role in preventing ER Ca^{2+} overload, and provided evidence that ORAI2 functions as a leak channel in the ER (Fig. 5D). The same single cell–based deconvolution approach that we introduce here can likely be used to identify molecular targets of drugs and their effect on dynamic regulatory mechanisms or to distinguish molecular causes of a disease that may differ within a patient population.

MATERIALS AND METHODS

Live-cell imaging

Extracellular buffer (ECB) contained 5 mM KCl, 125 mM NaCl, 1.5 mM $CaCl_2$, 1.5 mM $MgCl_2$, 10 mM D-glucose, and 20 mM Hepes (pH 7.4) and was supplemented freshly with probenecid (0.385 mg/ml) when Ca^{2+} dyes were used. Cells were loaded with 75 μl of Fluo-4 AM(1 μg/ml) or Fura-2 AM in the presence of F-127 (0.625 μl/ml) [20% solution in dimethyl sulfoxide (DMSO)] for 30 to 45 min, and then replaced with 50 μl of ECB. Hoechst 33342 (1 μg/ml) was in the loading buffer of Fluo-4 to provide a Fluo-4–independent mask for image analysis. Store-depletion traces were evoked by adding 50 μl of 8 mM EGTA and 4 μM thapsigargin in ECB. SOC was assayed 7.5 min later by adding 100 μl of 16 mM $CaCl_2$ and 2 μM thapsigargin in ECB. For the purpose of calibration, Fluo-4 was saturated by adding 200 μl of 10 μMionomycin, 2 μM thapsigargin, and 5 mM $CaCl_2$ at the end of every experiment. Hoechst 33342, Fluo-4 AM, Fura-2 AM, probenecid, F-127, and thapsigargin were from Invitrogen; ionomycin was from EMD Biosciences; and Hepes, DMSO, inorganic salts, and glucose were from Sigma. All Ca^{2+} imaging was done on an IX5000 automated epi-fluorescence microscope (Molecular Devices) equipped with a 4× S Fluor objective. Filters for Hoechst 33342 were D360/40× to D460/50m; Fluo-4, S470/30× to S510/30; and Fura-2, D340/12×, D360/10×, or D380/12× to D510/80m. For ER Ca^{2+} imaging by FRET, filters for CFP (cyan fluorescent protein) were S430/25 to 480/40; YFP (yellow fluorescent protein), S500/20 to S535/30; and FRET, S430/25 to S535/30. NCS1-mCherry was imaged on a custom-built spinning disc confocal microscope with a 100-mW, 593.5-nm solid-state laser (Changchun New Industries) with 594/10 excitation and 630/60 emission filters and an Apochromat 63× 1.4 numerical aperture oil objective (Carl Zeiss) mounted in an Axiovert 200M frame (Carl Zeiss) equipped with an Ultra VIEW spinning disk confocal scanner (PerkinElmer) and a CoolSNAP HQ CCD (charge-coupled device) camera (Photometrics).

Cell culture and transfection

NCS1 translocation experiments with HeLa cells were done in four-well Lab-Tek chambered coverslips (Nunc) coated with collagen (Advanced BioMatrix). All other experiments were done in 96-well plates (Corning) also coated with collagen. HEK293T cells were transfected with 75-ng siRNA using 0.2 μl of DharmaFECT I (Dharmacon) per well ~60 hours before imaging. Control cells were stained with 2.5 μM CMTPX (CellTracker Red, Invitrogen) in Opti-MEM I for 45 min, and then washed and quenched with Dulbecco's modified Eagle's medium + 10% fetal bovine serum for 45 min before all cells were replated on collagen a few hours before imaging. Cells that were transfected with targeting siRNA were treated identically, except that no CMTPX was mixed into Opti-MEM I. CMTPX had no effect on parameter estimates (fig. S4). Plasmids were transfected into HEK293T and HeLa cells with 3 μl of FuGENE 6 (Roche) per 1 μg of cDNA (complementary DNA) according to the manufacturer's instructions. For expression of PSEN2 in HEK293T cells or YFP–FKBP (FK505 binding protein)–INP54P in HeLa cells,

cells were transfected 24 hours before imaging. For expression of NCS1-mCherry in HeLa cells, cells were transfected 10 hours before imaging. The T1ER construct was co-transfected with siRNA using DharmaFECT Duo (Dharmacon).

cDNA constructs and siRNA

PSEN2 was amplified from the human ORFeome collection by polymerase chain reaction with primers 5′-ACTGCTCGAGATGCTCACATTCATGGCCTCTGAC-3′ (forward) and 5′-CAGTGAATTCTCAGATGTAGAGCTGATGGGAGG-3′ (reverse), cut with Xho I and Eco RI, and ligated into pIRES2-DsRed2-Express (Clontech). *ORAI2* was amplified with primers 5′-ACTGCTCGAGATGAGTGCTGAGCTTAACGTGCCT-3′ (forward) and 5′-CAGTGAATTCTCACAAGACCTGCAGGCTGCGC-3′ (reverse), cut with Xho I and Eco RI, and ligated into pIRES2-DsRed2-Express. INP54P was expressed as a fusion construct YFP-FKBP-INP54P, as described in (25). YFP-FKBP served as the control. *NCS1* was recombined from the human ORFeome collection into pmCherry-N-DEST/TO. T1ER was described in (11). The sequence of each construct was verified. Diced siRNA was synthesized according to a previously published protocol (26), with bacterial amp_R serving as control. Primer sequences are listed in table S1. Synthetic siRNAs targeting *PSEN2* with individual sequences 5′-GAGCGAAGCACGUGAUCAU-3′ (siPSEN2–4), 5′-GGAGGACCCUGACCGCUAU-3′ (siPSEN2-3), 5′-GAGCGGACGUCCCUAAUGU-3′ (siPSEN2-2), and 5′-CAUAUUCCCUGCCCUGAUA-3′ (PSEN2-1) and lamin A/C control siRNA(D-001050)were purchased from Dharmacon.

Parameter estimation

To identify the molecular parameters of the model (Fig. 2D) from single-cell traces, we formulated a prediction $h(t)$ for the ionomycin-calibrated Fluo-4 measurements as a function of cytosolic $[Ca^{2+}]_{cyt}$.

$$h(t)=\frac{[\mathrm{Ca}^{2+}]_{\mathrm{cyt}}(t)+K_{\mathrm{D}}F_{\mathrm{min}}}{K_{\mathrm{D}}+[\mathrm{Ca}^{2+}]_{\mathrm{cyt}}(t)} \quad (1)$$

K_D is the affinity of Fluo-4 for Ca^{2+}, and F_{min} is the fluorescence of Fluo-4 in the absence of Ca^{2+}. K_D and R were undetermined and scaled linearly with $[Ca^{2+}]_{cyt}$ or $[Ca^{2+}]_{ER}$, respectively. Because K_D and R had strictly no influence on the model other than scaling other parameters, those variables were always fixed. K_D = 1 μM is a widely used estimate for the affinity of Fluo-4 for intracellular Ca^{2+} (Fig. 2E) (27).

All other parameters p were determined by minimizing the discrepancy between model prediction $h(t_i; p)$ and actual Fluo-4 data η_i in the form of a least-squares functional with measurement errors σ_i:

$$\min_{p}\sum_{\mathrm{i}}\frac{(h(t_i;p)-\eta_{\mathrm{i}})^2}{\sigma_{\mathrm{i}}^2} \quad (2)$$

σ_i was assumed to be constant at 1% of maximal Fluo-4 fluorescence F_{max}. Equation 2 was minimized for each single-cell trace with a multiple-shooting Gauss-Newton–type algorithm implemented by PARFIT (5). The multiple-shooting approach discretizes the model trajectory, allowing it to initialize the model at each node close to the measurements and only then to consider boundary constraints. As a consequence, fast convergence, relative independence of initial guesses, and increased resistance to poor local optima can be

observed. The calculations were performed on a computer cluster assembled from 552 Intel E5345 processors with 2208 cores in total.

Representative population estimates shown in Fig. 2F are consistent with previous knowledge: F_{min} is often assumed to be F_{min} = 1/40 = 0.025. The value of $[Ca^{2+}]_{ER}(0)$ = 400 μM is obtained for a ratio of volume and buffering between ER and cytosol of R = 1/400, consistent with much larger cytoplasmic volume and buffering of Ca^{2+} than in the ER (28). Without correction for differences in volume and buffering, an effective concentration of 1 μM in the ER is consistent with the typical height of a cytosolic Ca^{2+} peak induced by rapid release from the ER with ionomycin. K_M = 200 nM and n = 2.1 are consistent with previously reported measurements for PMCA (9).

We calculated turnover at the ER membrane as $J_{ER} = k_{ER,leak}\,[Ca^{2+}]_{ER}(0)$ = 14 nM/s.

We calculated turnover at the PM by substituting a basal cytosolic calcium concentration of 70 nM for $[Ca^{2+}]_{cyt}(t)$ in:

$$J_{PM}=\frac{J_{max}\left[Ca^{2+}\right]^n_{cyt}(t)}{K^n_M+\left[Ca^{2+}\right]^n_{cyt}(t)}=0.8\mathrm{nM/s} \quad (3)$$

This model prediction that turnover at the ER is many times faster than at the PM is consistent with the interpretation that intracellular Ca^{2+} signaling can in the short term be described by rapid uptake and release from Ca^{2+} stores (29).

To measure J_{PM}, we recorded cytosolic calcium traces after Ca^{2+} was released from the ER by 1.25 μM ionomycin together with 1 μM thapsigargin to inactivate SERCA, and 5 mM extracellular EGTA. The slope of $[Ca^{2+}]_{cyt}$ was measured where $[Ca^{2+}]_{cyt}$ crossed K_M = 200 nM downwards, corresponding to the half-maximal extrusion capacity $J_{max}/2$. This measured J_{max} in the range of 10 nM/s was consistent with the parameter estimate from the model (Fig. 2E). k_{SOC} was not a model parameter and was instead measured for each cell as the initial slope of cytosolic Ca^{2+} when external Ca^{2+} was added back after store depletion.

Parameter uncertainty

We used the HYPERSPACE package (30) to sample the parameter space over two orders of magnitude around a representative parameter set (Fig. 2F and fig. S1, A and B). In addition, we characterized parameter uncertainty by a local measure based on the sensitivity of the measurement predictions h to the parameter values p. It can be shown that

$$C=\left(J^{\mathrm{T}}J\right)^{-1} \quad (4)$$

and is a linear approximation of the parameter covariance matrix with

$$J=-\Sigma^{-1}\frac{dh}{dp} \quad (5)$$

where Σ are the diagonalized measurement errors σ_i, and h are the vectorized model predictions at time points t_i (10). We used the VPLAN package (10) to compute C in fig. S1C or for different knockdown efficiencies in fig. S1, D and E. Figure S1C shows the eigenvalue spectrum λ of C in unperturbed cells and the orientation of the largest eigenvector in parameter space, suggesting that our model has similar properties with respect to parameter uncertainty compared to all those characterized in (4).

For siRNA experiments, population estimates of F_{min}, K_M, and n were determined from control cells in coculture with the goal to minimize the influence of experimental variability and systematic errors. For the screen in Fig. 4, we considered that such effects could vary between cells (for example, due to variable abundance of PMCA isoforms or effects of cell shape) and considered imperfect calibration of Fluo-4. To this end, we added regularization terms to the least-squares functional Eq. 2, yielding

$$\min_p\left(\sum_i\left(\frac{(h(t_i;p)-\eta_i)^2}{\sigma_i^2}\right)+\sum_k\left(\frac{(p_k-p_{k,0})^2}{\sigma_k^2}\right)\right) \quad (6)$$

and reintroduced $F_{max} = 1$ into Eq. 1, yielding

$$h(t)=\frac{F_{max}[Ca^{2+}]_{cyt}(t)+K_D F_{min}}{K_D+[Ca^{2+}]_{cyt}(t)} \quad (7)$$

p_k was the parameter F_{min}, K_M, n, or F_{max} regularized to $p_{k,0}$ (determined each from the control cells of the entire screen, or $F_{max,0} = 1$, respectively), each with an error estimate σ_k of 20%.

Supplementary Material

Refer to Web version on PubMed Central for supplementary material.

Acknowledgments

T7 RNA polymerase and Giardia Dicer were gifts from B.-O. Park. pmCherry-N-DEST/TO was contributed by A. Hayer. An *ORAI2* template was provided by the R. Dolmetsch Lab. We thank J. Schlöder, S. Körkel, and H. G. Bock for advice on the use of PARFIT and VPLAN. J. Ferrell, M. Covert, R. Dolmetsch, and many members of T.M.'s laboratory were helpful with comments. We appreciate practical help by A. Seki and K. Han. **Funding:** The Bio-X^2 cluster was funded by NSF award CNS-0619926 for computational resources. This work was supported by NIH grant GM030179 to T.M. and by the Swedish Society for Medical Research Postdoctoral Fellowship to S.M.

REFERENCES AND NOTES

1. Perelson AS, Neumann AU, Markowitz M, Leonard JM, Ho DD. HIV-1 dynamics in vivo: Virion clearance rate, infected cell life-span, and viral generation time. Science. 1996; 271:1582–1586. [PubMed: 8599114]
2. Cairns BJ, Timms AR, Jansen VAA, Connerton IF, Payne RJH. Quantitative models of in vitro bacteriophage-host dynamics and their application to phage therapy. PLoS Pathog. 2009; 5:e1000253. [PubMed: 19119417]
3. Kleiman LB, Maiwald T, Conzelmann H, Lauffenburger DA, Sorger PK. Rapid phospho-turnover by receptor tyrosine kinases impacts downstream signaling and drug binding. Mol. Cell. 2011; 43:723–737. [PubMed: 21884975]
4. Gutenkunst RN, Waterfall JJ, Casey FP, Brown KS, Myers CR, Sethna JP. Universally sloppy parameter sensitivities in systems biology models. PLoS Comput. Biol. 2007; 3:1871–1878. [PubMed: 17922568]
5. Bock HG, Kostina E, Schlöder JP. Numerical methods for parameter estimation in nonlinear differential algebraic equations. GAMM-Mitteilungen. 2007; 30:376–408.
6. Clapham DE. Calcium signaling. Cell. 2007; 131:1047–1058. [PubMed: 18083096]
7. Carrasco S, Meyer T. STIM proteins and the endoplasmic reticulum-plasma membrane junctions. Annu. Rev. Biochem. 2011; 80:973–1000. [PubMed: 21548779]
8. Thastrup O, Cullen PJ, Drøbak BK, Hanley MR, Dawson AP. Thapsigargin, a tumor promoter, discharges intracellular Ca^{2+} stores by specific inhibition of the endoplasmic reticulum Ca^{2+}-ATPase. Proc. Natl. Acad. Sci. U.S.A. 1990; 87:2466–2470. [PubMed: 2138778]

9. Bautista DM, Hoth M, Lewis RS. Enhancement of calcium signalling dynamics and stability by delayed modulation of the plasma-membrane calcium-ATPase in human T cells. J. Physiol. 2002; 541:877–894. [PubMed: 12068047]
10. Bauer I, Bock HG, Körkel S, Schlöder JP. Numerical methods for optimum experimental design in DAE systems. J. Comput. Appl. Math. 2000; 120:1–25.
11. Abell E, Ahrends R, Bandara S, Park BO, Teruel MN. Parallel adaptive feedback enhances reliability of the Ca^{2+} signaling system. Proc. Natl. Acad. Sci. U.S.A. 2011; 108:14485–14490. [PubMed: 21844332]
12. Brandman O, Liou J, Park WS, Meyer T. STIM2 is a feedback regulator that stabilizes basal cytosolic and endoplasmic reticulum Ca^{2+} levels. Cell. 2007; 131:1327–1339. [PubMed: 18160041]
13. Li YM, Lai MT, Xu M, Huang Q, DiMuzio-Mower J, Sardana MK, Shi XP, Yin KC, Shafer JA, Gardell SJ. Presenilin 1 is linked with γ-secretase activity in the detergent solubilized state. Proc. Natl. Acad. Sci. U.S.A. 2000; 97:6138–6143. [PubMed: 10801983]
14. Cruts M, Van Broeckhoven C. Presenilin mutations in Alzheimer's disease. Hum. Mutat. 1998; 11:183–190. [PubMed: 9521418]
15. Tu H, Nelson O, Bezprozvanny A, Wang Z, Lee SF, Hao YH, Serneels L, De Strooper B, Yu G, Bezprozvanny I. Presenilins form ER Ca^{2+} leak channels, a function disrupted by familial Alzheimer's disease-linked mutations. Cell. 2006; 126:981–993. [PubMed: 16959576]
16. Kasri NN, Kocks SL, Verbert L, Hébert SS, Callewaert G, Parys JB, Missiaen L, De Smedt H. Up-regulation of inositol 1,4,5-trisphosphate receptor type 1 is responsible for a decreased endoplasmic-reticulum Ca^{2+} content in presenilin double knock-out cells. Cell Calcium. 2006; 40:41–51. [PubMed: 16675011]
17. Brunello L, Zampese E, Florean C, Pozzan T, Pizzo P, Fasolato C. Presenilin-2 dampens intracellular Ca^{2+} stores by increasing Ca^{2+} leakage and reducing Ca^{2+} uptake. J. Cell. Mol. Med. 2009; 13:3358–3369. [PubMed: 19382908]
18. Shilling D, Mak DO, Kang DE, Foskett JK. Lack of evidence for presenilins as endoplasmic reticulum Ca^{2+} leak channels. J. Biol. Chem. 2012; 287:10933–10944. [PubMed: 22311977]
19. Takasugi N, Tomita T, Hayashi I, Tsuruoka M, Niimura M, Takahashi Y, Thinakaran G, Iwatsubo T. The role of presenilin cofactors in the γ-secretase complex. Nature. 2003; 422:438–441. [PubMed: 12660785]
20. Gwack Y, Srikanth S, Oh-Hora M, Hogan PG, Lamperti ED, Yamashita M, Gelinas C, Neems DS, Sasaki Y, Feske S, Prakriya M, Rajewsky K, Rao A. Hair loss and defective T- and B-cell function in mice lacking ORAI1. Mol. Cell. Biol. 2008; 28:5209–5222. [PubMed: 18591248]
21. Masuo Y, Ogura A, Kobayashi M, Masaki T, Furuta Y, Ono T, Takamatsu K. Hippocalcin protects hippocampal neurons against excitotoxin damage by enhancing calcium extrusion. Neuroscience. 2007; 145:495–504. [PubMed: 17257765]
22. Hendricks KB, Wang BQ, Schnieders EA, Thorner J. Yeast homologue of neuronal frequenin is a regulator of phosphatidylinositol-4-OH kinase. Nat. Cell Biol. 1999; 1:234–241. [PubMed: 10559922]
23. De Barry J, Janoshazi A, Dupont JL, Procksch O, Chasserot-Golaz S, Jeromin A, Vitale N. Functional implication of neuronal calcium sensor-1 and phosphoinositol 4-kinase-b interaction in regulated exocytosis of PC12 cells. J. Biol. Chem. 2006; 281:18098–18111. [PubMed: 16638749]
24. Missiaen L, Raeymaekers L, Wuytack F, Vrolix M, de Smedt H, Casteels R. Phospholipid- protein interactions of the plasma-membrane Ca^{2+}-transporting ATPase. Biochem. J. 1989; 263:687–694. [PubMed: 2532005]
25. Abe N, Inoue T, Galvez T, Klein L, Meyer T. Dissecting the role of PtdIns(4,5)P_2 in endocytosis and recycling of the transferrin receptor. J. Cell Sci. 2008; 121:1488–1494. [PubMed: 18411250]
26. Myers JW, Jones JT, Meyer T, Ferrell JE Jr. Recombinant dicer efficiently converts large dsRNAs into siRNAs suitable for gene silencing. Nat. Biotechnol. 2003; 21:324–328. [PubMed: 12592410]
27. Thomas D, Tovey SC, Collins TJ, Bootman MD, Berridge MJ, Lipp P. A comparison of fluorescent Ca^{2+} indicator properties and their use in measuring elementary and global Ca^{2+} signals. Cell Calcium. 2000; 28:213–223. [PubMed: 11032777]

28. Mogami H, Gardner J, Gerasimenko OV, Camello P, Petersen OH, Tepikin AV. Calcium binding capacity of the cytosol and endoplasmic reticulum of mouse pancreatic acinar cells. J. Physiol. 1999; 518:463–467. [PubMed: 10381592]

29. Meyer T, Stryer L. Molecular model for receptor-stimulated calcium spiking. Proc. Natl. Acad. Sci. U.S.A. 1988; 85:5051–5055. [PubMed: 2455890]

30. Zamora-Sillero E, Hafner M, Ibig A, Stelling J, Wagner A. Efficient characterization of high-dimensional parameter spaces for systems biology. BMC Syst. Biol. 2011; 5:142. [PubMed: 21920040]

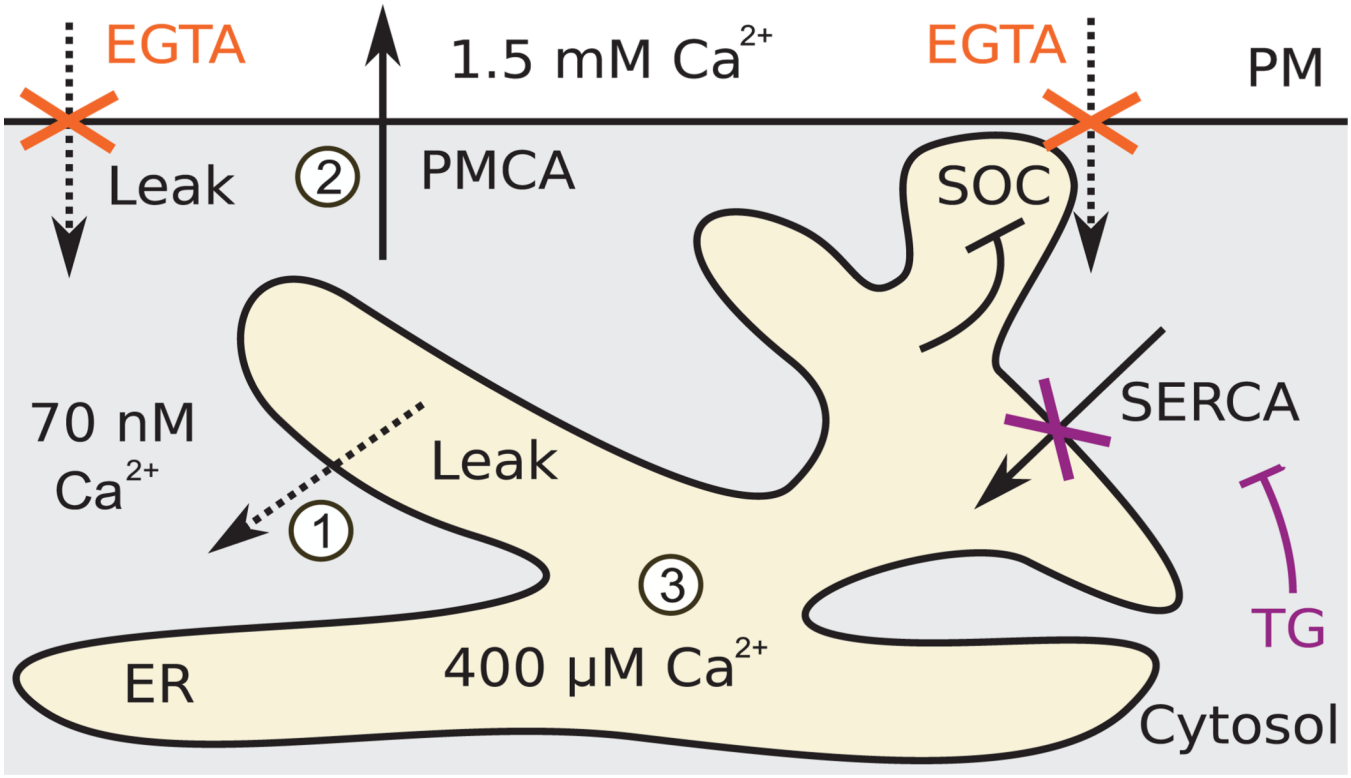

Fig. 1. Schematic of the core Ca^{2+} regulatory system

PM Ca^{2+} pump PMCA maintains a large gradient of Ca^{2+} across the PM. Ca^{2+} pump SERCA in the ER membrane fills an ER Ca^{2+} store that is used in rapid signaling events. Both pump proteins maintain these gradients against the effects of leak through regulated and constitutively active Ca^{2+} channels. Depletion of the ER Ca^{2+} store triggers influx of Ca^{2+} from the outside in a process termed SOC, which is inhibited by ER Ca^{2+}. Our experimental approach combined thapsigargin (TG) to block SERCA with EGTA to chelate external Ca^{2+}, thus blocking entry of Ca^{2+} from the outside. Dashed arrows indicate passive, but possibly regulated, leak. Solid arrows indicate ATP (adenosine 5′-triphosphate)–driven pump activities. Numbers in white circles reference model terms in Fig. 2D.

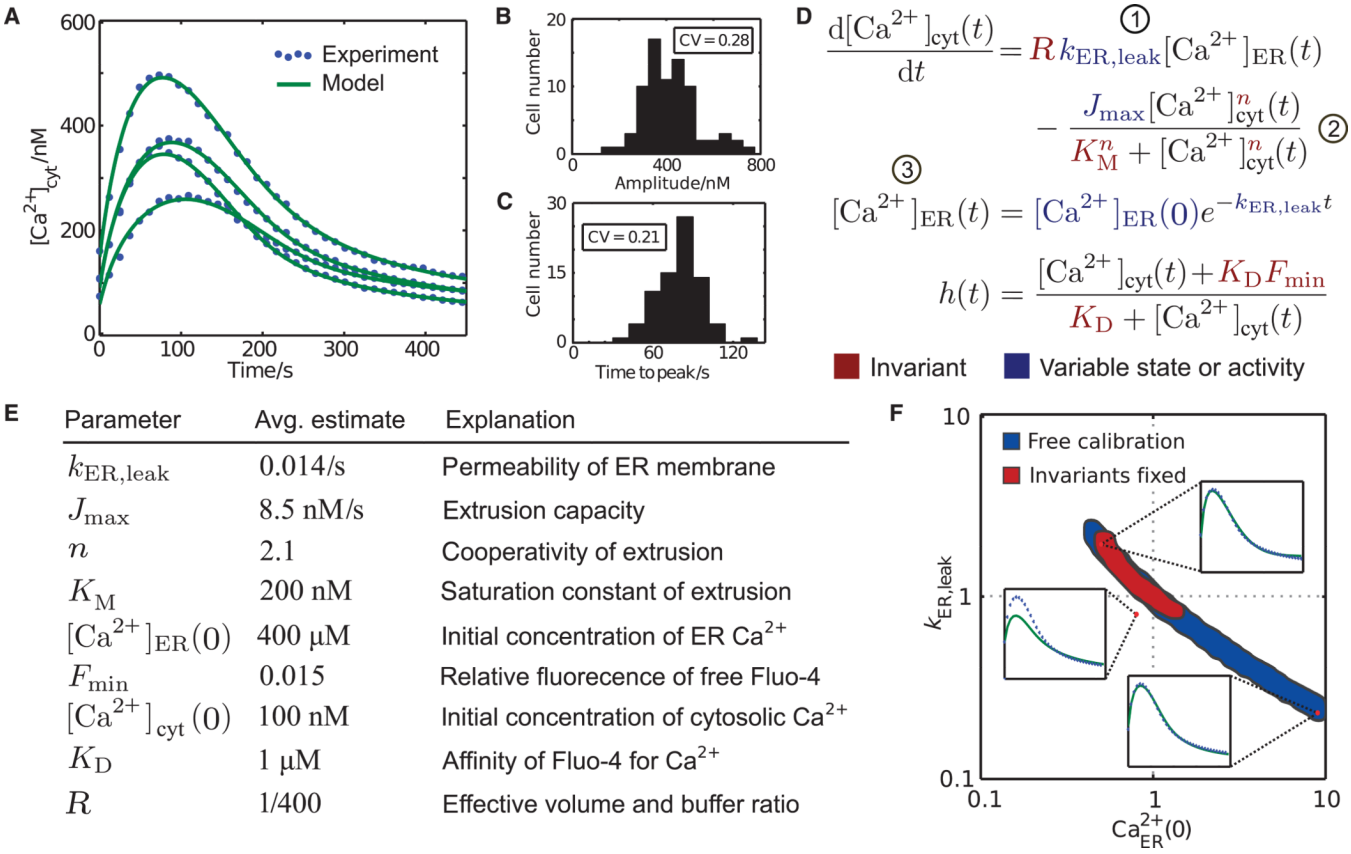

Parameter	Avg. estimate	Explanation
$k_{ER,leak}$	0.014/s	Permeability of ER membrane
J_{max}	8.5 nM/s	Extrusion capacity
n	2.1	Cooperativity of extrusion
K_M	200 nM	Saturation constant of extrusion
$[Ca^{2+}]_{ER}(0)$	400 μM	Initial concentration of ER Ca^{2+}
F_{min}	0.015	Relative fluorecence of free Fluo-4
$[Ca^{2+}]_{cyt}(0)$	100 nM	Initial concentration of cytosolic Ca^{2+}
K_D	1 μM	Affinity of Fluo-4 for Ca^{2+}
R	1/400	Effective volume and buffer ratio

Fig. 2. Extraction of molecular parameter values from time-resolved, single-cell Ca^{2+} measurements

(**A**) Single-cell Ca^{2+} responses upon addition of EGTA and thapsigargin. (**B** and **C**) Cell-to-cell variability of amplitude (B) and peak timing (C). CV, coefficient of variation. (**D**) Differential equations model that was used to infer parameter values. Numbers in circles denote terms illustrated in Fig. 1. (**E**) Population averages of single-cell parameter estimates. K_D and R were linear with $[Ca^{2+}]_{cyt}$ or $[Ca^{2+}]_{ER}(0)$, respectively, and thus were always fixed (see Materials and Methods). (**F**) Exemplary slice through the seven-dimensional parameter space in which parameter sets were projected onto the plane spanned by the axes of ER leak ($k_{ER,leak}$) and the initial concentration of ER Ca^{2+} [$Ca^{2+}{}_{ER}(0)$]. Blue shading indicates the range of fold changes away from a simulated "true" parameter set in the center for which nearly identical fits could be obtained when all parameters were variable. Red shading shows the reduced range of parameters when the invariant parameters n, K_M, and F_{min} were constrained. The upper right and lower left insets show examples of parameter combinations that fit the same data. The upper left inset shows an example where this is not the case despite much smaller deviation from the true parameter set than the other two example parameter combinations.

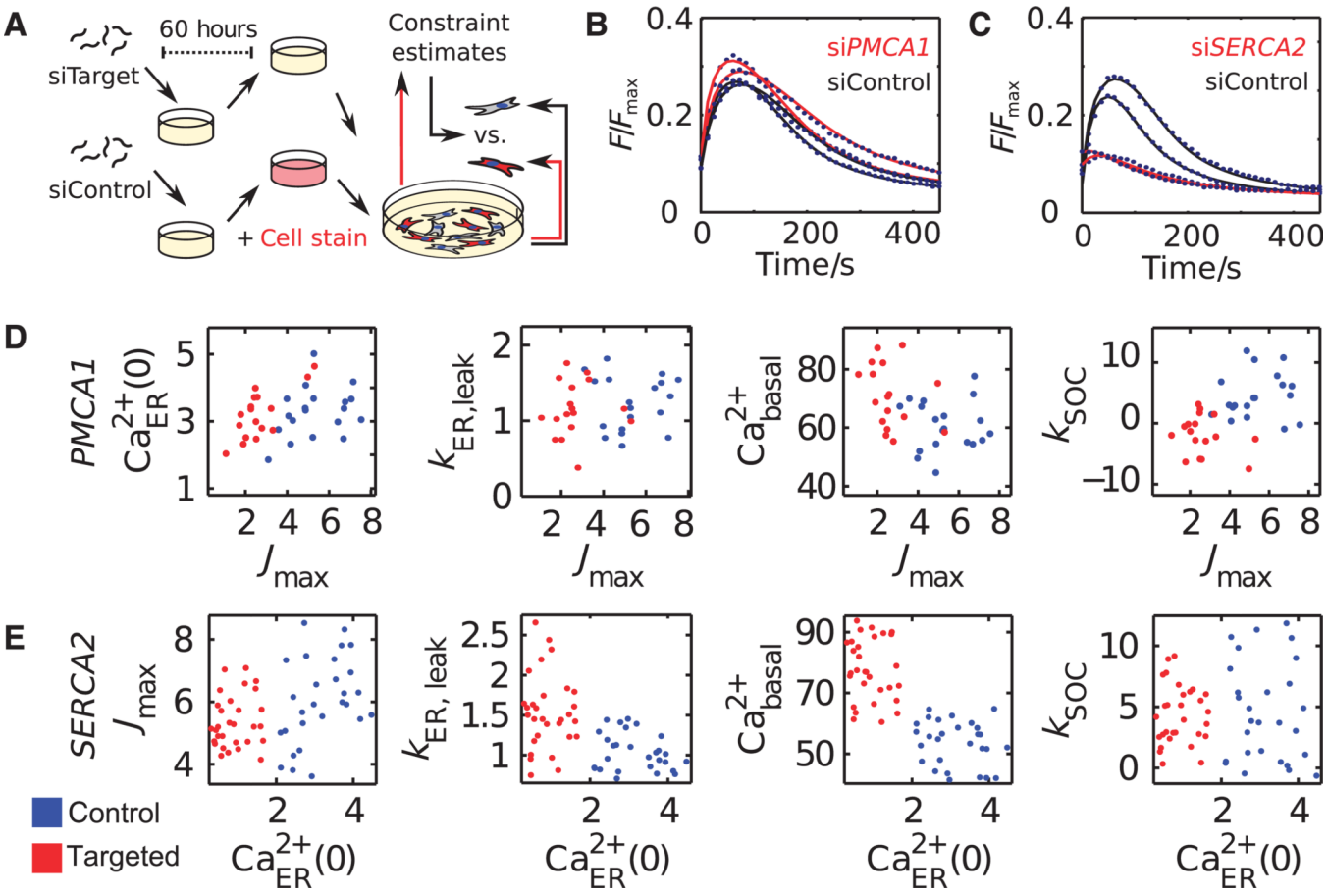

Fig. 3. Mapping of siRNA effects into a molecular parameter space of protein function

(**A**) Coculture assay used to constrain the parameter estimation problem. (**B** and **C**) Single-cell calcium traces of control cells and cells expressing siRNA targeting *PMCA1* (B) or *SERCA2* (C). (**D** and **E**) Single-cell parameter estimates from cells in which PMCA1 (D) or SERCA2 (E) was knocked down (red) or from control cells (blue). Center 80% values from each condition are shown.

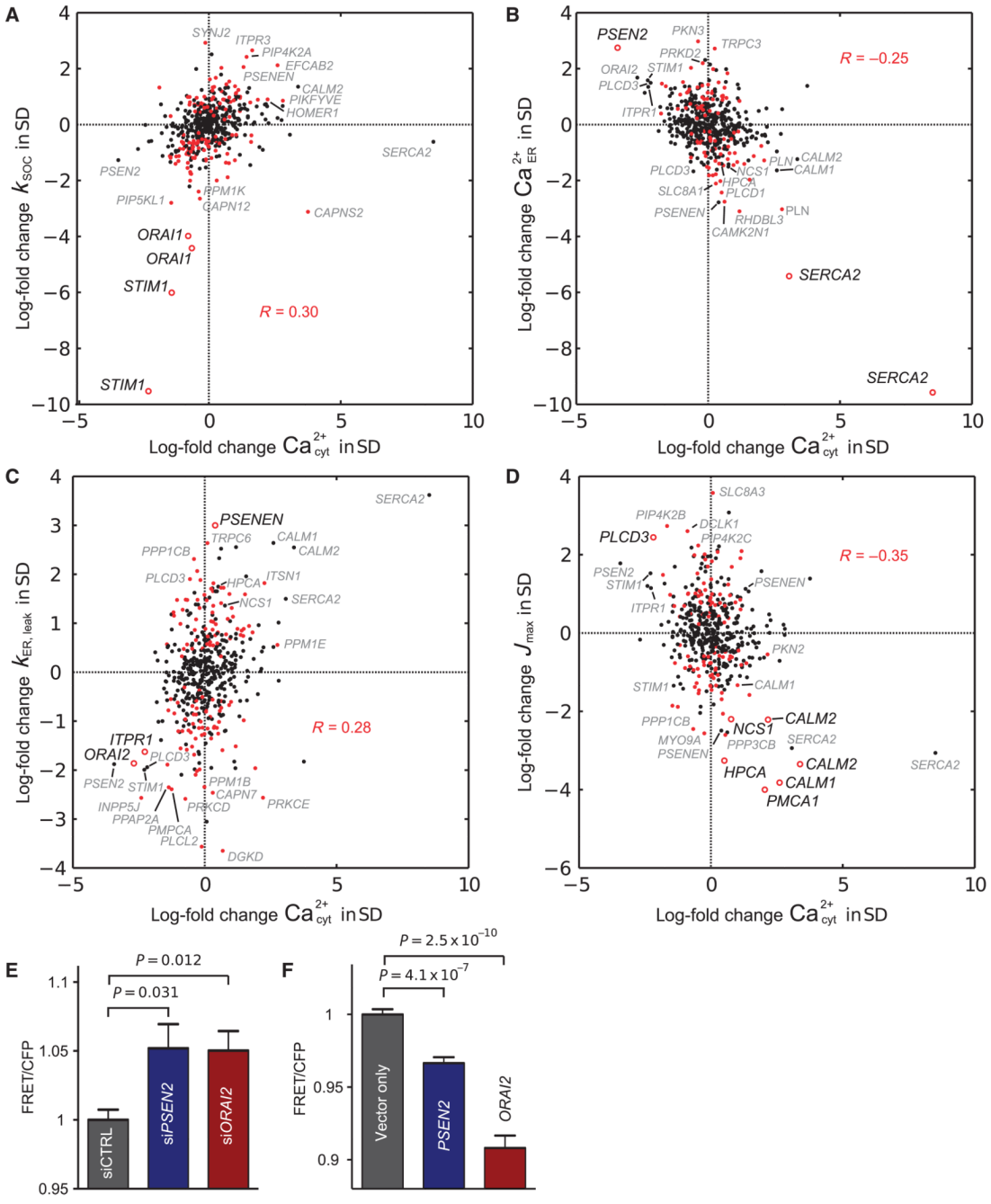

Fig. 4. Five-dimensional parameter analysis of an siRNA screen and validation of model predictions for the roles of PSEN2 and ORAI2

(**A** to **D**) Projections of the five-dimensional parameter readout onto the planes of basal cytosolic Ca^{2+} and (A) store-operated Ca^{2+} influx k_{SOC}, (B) initial ER load $Ca^{2+}{}_{ER}(0)$, (C) ER Ca^{2+} leak $k_{ER,leak}$, and (D) extrusion capacity J_{max} are shown as log-fold changes relative to control cells, median-centered and normalized per replicate by the SD σ along each dimension. Red data points denote siRNA effects that changed the parameters predominantly along the respective dimension shown in (A), (B), (C), or (D). Parameter changes labeled with the name of the targeted gene were outliers with $|\sigma| > 2.1$ or were predicted to have functional changes of $|\sigma| > 1$ due to secondary effects or because they were

one of a pair of replicates that was below the threshold. Parameter changes further analyzed and discussed in the text are indicated by open red circles and are labeled with emphasis in the projection where the primary change in function was observed. (**E** and **F**) FRET ratios showing differences in resting ER Ca^{2+} concentrations in cells when PSEN2 or ORAI2 was knocked down (E; $n = 12$) or overexpressed (F; $n \geq 22$). Shown are Bonferroni-corrected *P* values from two-tailed Student's *t* test; error bars show SEM.

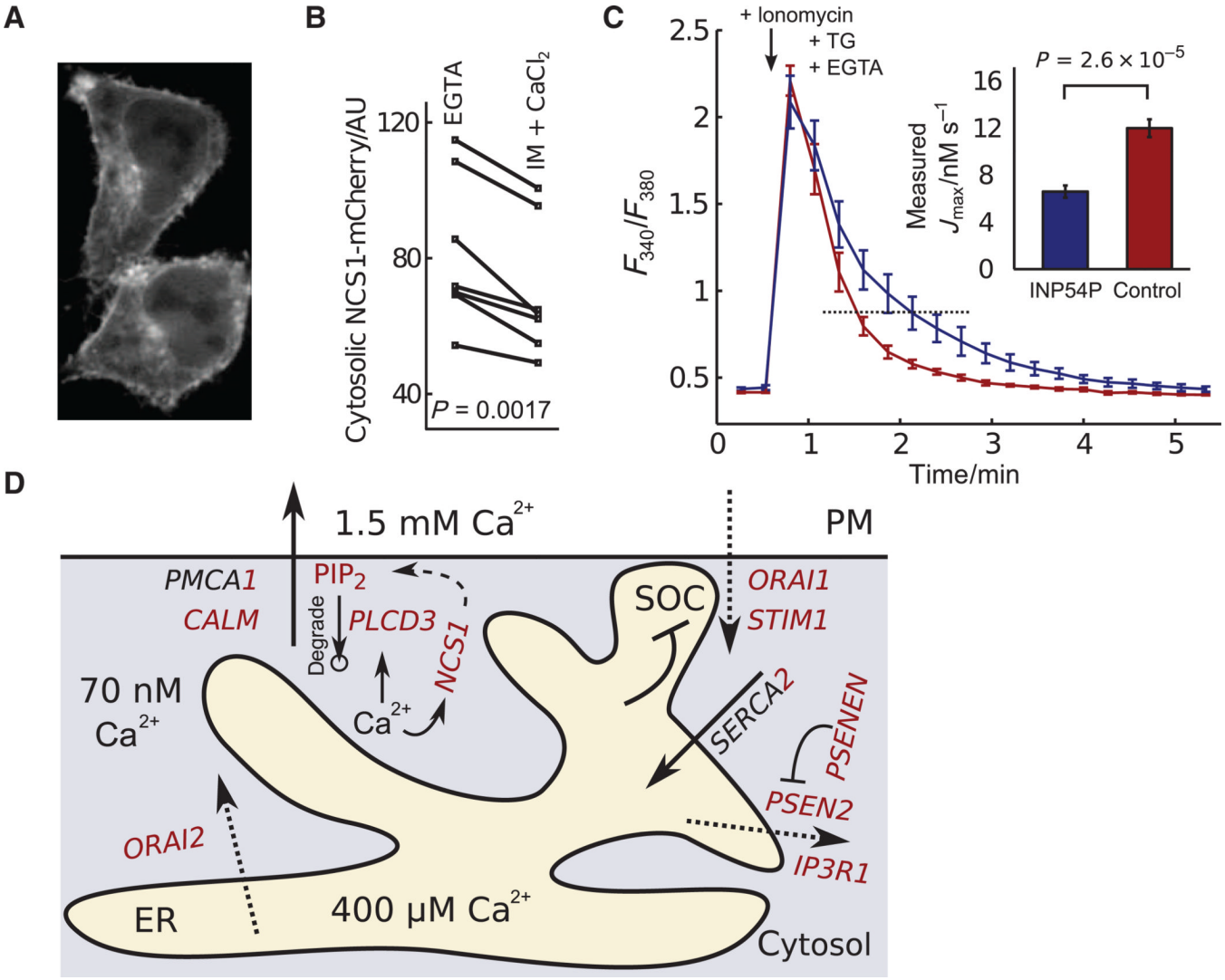

Fig. 5. PI(4,5)P_2 regulates Ca^{2+} extrusion and a more detailed model of the Ca^{2+} regulatory system

(**A**) PM localization of NCS1-mCherry increased when cytosolic Ca^{2+} was raised (see also movie S1). (**B**) Quantification comparing NCS1 localization in low and high cytosolic Ca^{2+} (*P* value from two-tailed paired Student's *t* test, $n = 7$). AU, arbitrary unit. (**C**) Fura-2 measurements of Ca^{2+} extrusion after rapid release from the ER by ionomycin. Inset shows quantification of the effect of reducing PI(4,5)P_2 abundance by INP54P overexpression on Ca^{2+} extrusion (*P* value from two-tailed Student's *t* test, $n \geq 6$; error bars show SEM). (**D**) More detailed molecular model of the Ca^{2+} regulatory systeminHEK293T cells. Specific isoforms and regulators are shown with their predicted functions derived from our computational analysis of time-course differences in the siRNA perturbation experiments. The circle below PIP_2 represents a sink resulting from the degradation of this molecule. PIP_2, PI(4,5)P_2.